

CECILIA: Direct O, N, S, and Ar Abundances in Q2343-D40, a Galaxy at $z \sim 3$

NOAH S. J. ROGERS,¹ ALLISON L. STROM,^{1,2} GWEN C. RUDIE,³ RYAN F. TRAINOR,⁴ MENELAOS RAPTIS,⁴ AND
CAROLINE VON RAESFELD^{1,2}

¹Center for Interdisciplinary Exploration and Research in Astrophysics (CIERA), Northwestern University, 1800 Sherman Ave., Evanston, IL, 60201, USA

²Department of Physics and Astronomy, Northwestern University, 2145 Sheridan Road, Evanston, IL 60208, USA

³Carnegie Observatories, 813 Santa Barbara Street, Pasadena, CA 91101, USA

⁴Department of Physics and Astronomy, Franklin & Marshall College, 637 College Avenue, Lancaster, PA 17603, USA

(Accepted to ApJL on March 1st, 2024)

ABSTRACT

Measurements of chemical abundances in high- z star-forming (SF) galaxies place important constraints on the enrichment histories of galaxies and the physical conditions in the early universe. JWST is beginning to enable direct chemical abundance measurements in galaxies at $z > 2$ via the detection of the faint T_e -sensitive auroral line [O III] λ 4364. However, abundances of other elements (e.g., S and Ar) in high- z galaxies remain unconstrained due to a lack of T_e data and wavelength coverage. Here, we present multiple direct abundances in Q2343-D40, a galaxy at $z = 2.9628 \pm 0.0001$ observed with JWST/NIRSpec as part of the CECILIA program. We report the first simultaneous measurement of T_e [O III] and T_e [S III] in a high- z galaxy, finding good agreement with the temperature trends in local SF systems. We measure a gas-phase metallicity of $12 + \log(\text{O}/\text{H}) = 8.07 \pm 0.06$, and the N/O abundance, $\log(\text{N}/\text{O}) = -1.37 \pm 0.21$, is indicative of primary nucleosynthesis. The S/O and Ar/O relative abundances, $\log(\text{S}/\text{O}) = -1.88 \pm 0.10$ and $\log(\text{Ar}/\text{O}) = -2.80 \pm 0.12$, are both > 0.3 dex lower than the solar ratios. However, the relative $\text{Ar}^{2+}/\text{S}^{2+}$ abundance is consistent with the solar ratio, suggesting that the relative S-to-Ar abundance does not evolve significantly with redshift. Recent nucleosynthesis models find that a significant amount of S and Ar are produced in Type Ia supernovae, such that the S/O and Ar/O abundances in Q2343-D40 could be the result of predominantly core-collapse supernovae enrichment. Future JWST observations of high- z galaxies will uncover whether S/O and Ar/O are sensitive to the timescales of these different enrichment mechanisms.

1. INTRODUCTION

The buildup of heavy elements is a direct consequence of galaxy evolution. Episodes of star formation produce massive stars, which in turn synthesize heavy metals through stellar nucleosynthesis. By means of mass-loss events and supernovae, the products of stellar nucleosynthesis are returned to the interstellar medium (ISM). These metals mix with the ISM and accreting gas, resulting in an increased gas-phase abundance that is imprinted in the next generation of stars. Therefore, the gas-phase metal abundance is sensitive to the past star formation, gas inflows and outflows, and ISM mixing mechanisms within a galaxy (e.g., Tosi 1988; Roy & Kunth 1995; Berg et al. 2019). Chemical abundance trends are of particular importance at high- z , as they provide insight into the gas-phase conditions in the early universe that give rise to the galaxy scaling relations observed today (such as the mass-metallicity relation, Lequeux et al. 1979; Tremonti et al. 2004; Erb et al. 2006).

Additionally, the relative abundances of different elements provides insight into the star-formation history of a galaxy

and nucleosynthetic mechanisms that operate on different timescales. For instance, O is produced in massive stars and returned to the ISM on short timescales via core-collapse supernovae (CCSN), such that gas-phase O/H traces the enrichment from massive stars. Massive stars also synthesize elements like Ne, S, and Ar through the α process. If this is the principal process by which these elements are produced, then the relative α element abundances (e.g., Ne/O) will be independent of the overall gas-phase metallicity (i.e., O/H). While N is synthesized in massive stars, N also has a secondary, metallicity-sensitive enrichment mechanism from intermediate-mass stars (Henry et al. 2000). Consequently, the N/O relative abundance is dependent on both the enrichment from stars of different masses and the overall metallicity of the ISM. Finally, Fe is produced in CCSN and Type Ia SNe; while Type Ia SNe contribute significantly to the overall Fe abundance, the timescale required for Type Ia enrichment is much longer than CCSN. This combination makes Fe/H sensitive to the prior star-formation history, and the α/Fe ratio

is dependent on the relative enrichment of CCSN and Type Ia SNe.

Reliable chemical abundances can be measured from the collisionally-excited lines (CELs) of metal ions in the ISM. The relative intensity of two CELs originating from different energy levels in the same metal ion is sensitive to gas-phase physical conditions such as the electron gas temperature T_e and electron density n_e . With these conditions, ionic abundances in the ISM can be directly calculated from the intensity and emissivity of metal CELs. While the intense “nebular” CELs can consistently be observed even in high- z nebulae (e.g., Bunker et al. 2023; Nakajima et al. 2023; Williams et al. 2023), the “direct” abundance method (Dinerstein 1990) relies on the simultaneous measurement of these CELs and faint, T_e -sensitive auroral lines in the rest-frame optical. Despite observational challenges associated with this technique, including potential biases in the presence of T_e and n_e variations (e.g., Peimbert 1967; Rubin 1989; Méndez-Delgado et al. 2023b,a), the direct method continues to be an important and successful tool for understanding the chemical enrichment of the local universe (e.g., Kennicutt et al. 2003; Esteban et al. 2004; Bresolin 2011; Berg et al. 2015; Arellano-Córdova et al. 2020; Rogers et al. 2022, among many others).

Until recently, the direct abundance method was difficult to apply in distant sources. At $z \sim 1$, the strong [O III] CELs redshift into the near-infrared (NIR) and the [O III] auroral line becomes exceedingly faint in low surface brightness sources. The same is true for the rest-frame NIR lines of [S III] and [Ar III]: the highest redshift measurements of direct S^{2+}/H^+ and Ar^{2+}/H^+ using these emission lines are in ionized regions at $z \lesssim 0.3$ (e.g., Izotov et al. 2021) and $z < 0.1$ (Dors et al. 2023), respectively. While measurements of T_e [O III] and direct O/H abundances have been acquired in individual galaxies at $z > 1$ through transmission windows in the NIR (see samples in Sanders et al. 2020; Clarke et al. 2023) and from UV spectroscopy of highly lensed systems (e.g., James et al. 2014; Citro et al. 2023), statistically significant samples of direct O/H abundances (let alone abundances from other elements such as N and S) have been challenging to acquire.

However, with the NIR capabilities of the *James Webb Space Telescope* (JWST), direct T_e measurements and abundances are now readily accessible in high- z galaxies (e.g., Arellano-Córdova et al. 2022a; Schaerer et al. 2022; Trump et al. 2023; Sanders et al. 2023a; Laseter et al. 2023; Welch et al. 2024; Topping et al. 2024). While these studies have started to uncover the chemical abundance patterns in the early universe, the current scope of high- z chemical abundances is still fairly limited. First, it is often the case that only a single auroral line, [O III] λ 4364, is available in the spectra of high- z star-forming galaxies. This auroral line permits a direct measurement of T_e [O III], which primarily

traces the gas containing high-ionization ions such as O^{2+} and Ne^{2+} . However, a lack of T_e in other ionization zones can significantly bias direct abundance measurements (Arellano-Córdova & Rodríguez 2020; Rogers et al. 2022). Particularly, robust S^{2+} and Ar^{2+} abundances require a measurement of T_e [S III], which has not been made in a galaxy at $z > 0.2$. Second, these prior surveys have focused mainly on the gas-phase O/H abundance and the relative Ne/O abundance if [Ne III] λ 3870 is detected. Measuring the abundance of other elements (e.g., N, S, and Ar) in high- z galaxies requires both deep spectroscopy and broad NIR wavelength coverage.

The CECILIA program (Strom et al. 2023) is poised to contribute detailed measurements of high- z T_e and ionic abundances from numerous ions. CECILIA uses the G235M and G395M gratings of NIRSpec and targets star-forming galaxies at $z > 2$ for ultra-deep NIR spectroscopy, enabling the detection of the [S III] λ 6314 and [O II] λ 7322,7332 auroral lines and strong NIR lines of [N II], [S II], [S III], and [Ar III]. Within this sample, the galaxy Q2343-D40 is of particular interest. Owing to Q2343-D40’s spectroscopic redshift of $z \sim 3$, simultaneous measurements of T_e [O III], T_e [S III], and robust ionic abundances are possible from the NIRSpec data. Here, we report the physical conditions (T_e [O III], T_e [S III], and n_e [S II]) and chemical abundances of O, N, S, and Ar in Q2343-D40, a star-forming galaxy ~ 2 Gyr after the Big Bang. This manuscript is organized as follows: in §2 we briefly summarize the data reduction, emission line fitting, and reddening corrections applied to the Q2343-D40 spectrum; the T_e , n_e , ionic abundance, ionization correction factors (ICFs), and total abundance calculations are described in §3; we compare Q2343-D40’s direct abundance trends to local star-forming systems and discuss these findings in §4; we summarize our conclusions in §5. Although all reported abundances are T_e -based, direct abundances refer to those that are derived from a measured T_e , while inferred abundances are those determined through application of a T_e - T_e relation or ICF. In this work, we assume a Λ CDM cosmology with $H_0 = 70 \text{ km s}^{-1} \text{ Mpc}^{-1}$, $\Omega_m = 0.3$, and $\Omega_\Lambda = 0.7$. We adopt the solar abundance values from Asplund et al. (2021): $12 + \log(O/H)_\odot = 8.69 \pm 0.04$ dex, $\log(N/O)_\odot = -0.86 \pm 0.08$ dex, $\log(S/O)_\odot = -1.57 \pm 0.05$ dex, and $\log(Ar/O)_\odot = -2.37 \pm 0.11$ dex. Throughout the text, we refer to emission lines using their vacuum wavelengths.

2. OBSERVATIONS AND REDUCTION

Q2343-D40 (R.A.=23h46m22.8s, Decl.=12°49′32″.1), hereafter D40, was observed as part of the CECILIA program, which targeted rest-UV color-selected star-forming galaxies in the Keck Baryonic Structure Survey (KBSS, Steidel et al. 2010; Rudie et al. 2012; Trainor et al. 2015; Strom et al. 2017). We briefly highlight the most important aspects

of the observations here and refer the reader to [Strom et al. \(2023\)](#) for the details concerning sample selection, exposure time requirements, and data reduction. Two NIRSpec grating combinations were used: G235M ($R \sim 1000$, $1.66\text{--}3.07\mu\text{m}$) data were acquired with a 29.5 hour exposure time to reliably detect the [S III] $\lambda 6314$ and [O II] $\lambda 7322, 7332$ auroral lines; G395M ($R \sim 1000$, $2.87\text{--}5.10\mu\text{m}$) data, necessary to detect [S III] $\lambda \lambda 9071, 9533$ for targets at $z \gtrsim 2.4$, were taken with an exposure time of 1.1 hours.

While the G235M data reduction was described in [Strom et al. \(2023\)](#), there have been significant improvements to the calibration files in recent versions of the CALWEBB pipeline, including updated reference pixels and bar shadow reference file for the MSA data. We reran the CALWEBB pipeline using version 1.12.5 (CRDS_CONTEXT = jwst_1180.pmap, [Bushouse et al. 2023](#)), MSAEXP version 0.6.11 ([Brammer 2022](#)), and GRIZLI version 1.8.9 ([Brammer 2023](#)). We use NSCLEAN ([Rauscher 2023](#)) to correct for $1/f$ noise. However, we observed that running NSCLEAN with default parameters introduced residual noise artifacts in the G235M and G395M rate files. Updating the critical frequency to $fc=1/2048$, the kill width to $kw=fc/4$, and the Gaussian smoothing standard deviation to $buffer_sigma=3$ removed the $1/f$ noise while decreasing the residual RMS noise in the individual rate files.

Background subtraction was completed using a global background solution based on all available MSA slits (masking pixels illuminated by the science targets) for both G235M and G395M data (similar to [Strom et al. 2023](#)). To ensure reliable extractions of the science spectra, we fit and subtract the residual background in D40’s 2D spectra with a low-order polynomial in the dispersion direction. 1D science spectra are extracted using the default MSAEXP Gaussian extraction model. Despite these updates, there are persistent flux calibration issues in the NIRSpec data. To account for these, we rescale the G235M spectrum to match the best-fit model spectral energy distribution (SED) of D40. The SED fit is based on existing optical (U_n , G , and \mathcal{R}) and NIR (H and K_s) photometry, as well as imaging using *Hubble Space Telescope*/WFC3 F140W. We calculate the ratio of the SED and NIRSpec spectrum, then fit this ratio with a quadratic polynomial as a function of wavelength while excluding emission lines. This flux rescaling function, $f_{corr}(\lambda)$, is used to scale the G235M spectrum to the SED continuum (similar to the approach taken by [Arrabal Haro et al. 2023](#)).

Estimating a similar flux rescaling function for the G395M data is challenging owing to the weaker continuum with higher RMS noise. Instead, we use the spectral region that is coincident between G235M and G395M to scale the G395M continuum to the G235M continuum. We note that these flux differences between the two gratings could be due to a combination of flux calibration issues and the wavelength-

dependent point spread function. For the following analysis, we use line flux ratios within individual filters to avoid potential systematic errors associated with the cross-band flux calibration. The redshift of D40 was uncertain prior to the NIRSpec observations, but we determine the spectroscopic redshift of D40 to be $z=2.9628 \pm 0.0001$ using 11 strong emission lines.

The final reduced rest-frame spectrum of D40 is plotted in [Figure 1](#), where the strong nebular lines are highlighted by vertical dotted lines in each panel. Emission lines are fit using a linear continuum and Gaussian profile: the G235M (G395M) spectrum is split into 9 (7) windows, where a constant full-width at half maximum (FWHM) and velocity offset are used for all lines in a given window. This procedure allows for a fit to emission lines that are blended at NIRSpec’s resolution (e.g., [Ar IV] $\lambda 4713$ and He I $\lambda 4715$). To account for stellar absorption, the Balmer lines are fit with Gaussian profiles and the best-fit SED continuum, which shows relatively low Balmer absorption equivalent width ($\lesssim 3.5 \text{ \AA}$). We repeated the analysis using the SED continuum for all emission line fits and find that the results are consistent with the linear continuum+Gaussian emission line approach. Therefore, we adopt the linear continuum+Gaussian line model for all other emission lines to allow for a more flexible fit to the local continuum. We measure the RMS noise in continuum windows on either side of the emission line, then calculate the line flux uncertainty as $\delta F(\lambda) = 2 \times \sqrt{n_{pix}} \times RMS$, where n_{pix} is the number of pixels within ± 1 FWHM from the line center (see [Berg et al. 2013](#)). Although this does not account for the uncertainty in the absolute flux calibration, the analysis presented here focuses on the ratios of line fluxes.

To estimate the relative flux uncertainties, we utilize the G235M $f_{corr}(\lambda)$ functions for the 23 CECILIA galaxies reported in [Strom et al. \(2023\)](#). We normalize each galaxy’s $f_{corr}(\lambda)$ function at the wavelength of $H\beta$ measured in D40, or $1.93\mu\text{m}$. For the full sample, we calculate the standard deviation in $f_{corr}(\lambda)/f_{corr}(1.93\mu\text{m})$ as a function of wavelength. We find that the standard deviation measured from the ensemble of $f_{corr}(\lambda)/f_{corr}(1.93\mu\text{m})$ is relatively constant and $\lesssim 6\%$ at a given wavelength. As such, we assume that a constant 6% uncertainty on all flux ratios relative to $H\beta$ provides a reasonable approximation on the relative flux calibration uncertainty. This uncertainty is added in quadrature to the uncertainty on all emission line flux ratios before calculating physical conditions. An emission line is considered detected if $F(\lambda)/F(H\beta)$ has a signal-to-noise (S/N) > 3 .

To correct for dust attenuation, we first account for attenuation along the line of sight to D40. The foreground reddening, $E(B-V)=0.037$, was retrieved from the [Schlegel et al. \(1998\)](#) dust maps using the PYTHON DUSTMAPS package ([Green 2018](#)) and the position of D40. The observed spectrum is corrected for foreground extinction using the [Cardelli](#)

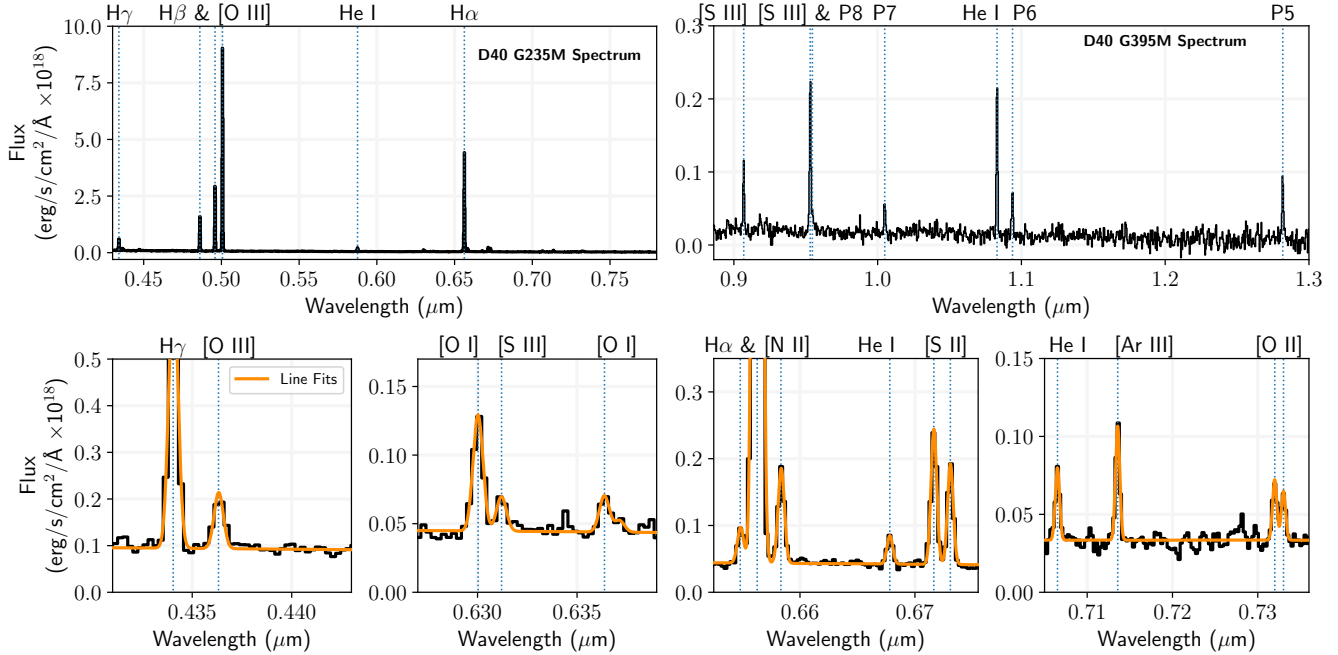


Figure 1. The redshift-corrected NIRSpectra of D40. The top two panels provide the full spectral range of the G235M (left) and G395M (right) spectra, while panels in the bottom row highlight the faint emission lines detected in the G235M spectrum. In each panel, key spectral features are denoted with vertical dotted lines. The Gaussian+linear continuum fits to the emission lines are shown in orange. The auroral lines [O III] λ 4364 and [S III] λ 6314 are detected at high significance, producing the data required to measure, for the first time in a high- z galaxy, simultaneous T_e [O III] and T_e [S III] and the gas-phase abundances from N, O, S, and Ar.

et al. (1989) Galactic attenuation law with $R_V=3.1$. Although the Cardelli et al. (1989) is only calibrated to $3.3\mu\text{m}$, the low foreground attenuation makes this correction relatively small for D40 (i.e., the maximum correction within the G235M spectrum is a $\sim 2\%$ increase in the flux of $H\gamma$). We use the PYTHON PYNEB (Luridiana et al. 2012, 2015) package’s GETCORR function to perform the correction for foreground attenuation.

Next, we determine $E(B-V)$ due to dust attenuation within D40 using the Reddy et al. (2020) quadratic nebular attenuation law. This law has been calibrated on the Balmer line emission in star-forming galaxies at $1.4 \leq z \leq 2.6$ from the MOSFIRE Deep Evolution Field survey (Kriek et al. 2015), which should better characterize the general trends of dust attenuation for high- z galaxies. The shape of the Reddy et al. (2020) law is similar to that of the Cardelli et al. (1989) Galactic attenuation law and implies an R_V of 3.09. Future JWST spectroscopic observations will better constrain the shape of the dust attenuation law at high- z and will assess whether its functional form deviates significantly from the frequently utilized Galactic attenuation law (see recent work by Markov et al. 2024).

The best-fit $E(B-V)$ is calculated as a weighted average from the $E(B-V)$ predicted by the observed $H\alpha/H\beta$ and $H\gamma/H\beta$ ratios. Both Balmer line ratios are compared to their predicted intensity ratios from Storey & Hummer (1995) as-

suming Case B recombination at $T_e=1.2 \times 10^4$ K and $n_e=10^2$ cm^{-3} . For each ratio, uncertainty is estimated by recalculating $E(B-V)$ for a distribution of 500 ratios with center and standard deviation equal to the measured line ratio and its uncertainty, respectively. $H\alpha/H\beta$ and $H\gamma/H\beta$ indicate $E(B-V)=0.09 \pm 0.06$ and 0.19 ± 0.10 , respectively, in statistical agreement. The weighted average is $E(B-V)=0.12 \pm 0.05$. We use the PYNEB GETCORRH function to perform the reddening correction relative to $H\beta$ for the emission line ratios in the G235M spectrum, and propagate the uncertainties on the relative line fluxes and $E(B-V)$ to obtain uncertainties on the line intensity ratios. We report the reddening-corrected G235M line intensities relative to $H\beta$ in Table 1.

The relative Paschen line ratios measured in the G395M spectrum indicate that a flux calibration issue is still present in the data. For example, the measured P8/P6, P7/P6, and P6/P5 ratios are all greater than the theoretical ratios at $T_e=1.2 \times 10^4$ K and $n_e=10^2$ cm^{-3} , the opposite trend that is expected from dust reddening. Additionally, the P8/ $H\beta$ ratio agrees with the theoretical ratio, indicating negligible reddening in the NIR spectrum which is at odds with the optical Balmer line ratios. As such, we do not use the Paschen-to- $H\beta$ ratios for reddening correction in D40. However, for the following T_e and abundance analysis we only require the strong lines of [S III]. In particular, [S III] λ 9533 neighbors P8 at 9549 \AA , such that their relative fluxes should

be insensitive to both dust attenuation and the effects of wavelength-dependent flux calibration issues. We use the theoretical P8/H β ratio (0.036 at $T_e=1.2\times 10^4$ K and $n_e=10^2$ cm $^{-3}$, Storey & Hummer 1995) and the [S III] λ 9533/P8 flux ratio to obtain an estimate on [S III] λ 9533/H β that is roughly corrected for reddening and flux calibration uncertainties. The resulting line ratio is $I([\text{S III}]\lambda 9533)/I(\text{H}\beta) = 0.29\pm 0.03$, where we have assumed a 6% relative flux uncertainty for [S III] λ 9533/P8 before correcting to the H β flux.¹ This line intensity ratio is used in the derivation of $T_e[\text{S III}]$ and S^{2+}/H^+ in the following section. We include the G395M line flux ratios relative to F(P8) in Table 1, where we also include the inferred intensity ratios relative to H β for lines in close proximity to P8.

3. PHYSICAL CONDITIONS, IONIC AND TOTAL ABUNDANCES

3.1. Electron Temperature and Density

To directly calculate the gas-phase chemical abundances in D40, we assume a three-zone ionization model. The low-ionization zone contains O $^+$, N $^+$, and S $^+$, with ionization potentials (IPs) 13.6 eV, 14.5 eV, and 10.4 eV, respectively; the intermediate-ionization zone contains S $^{2+}$ (IP=23.3 eV) and Ar $^{2+}$ (IP=27.6 eV); the high-ionization zone contains O $^{2+}$ (IP=35.1 eV) and Ar $^{3+}$ (IP=40.7 eV). We provide the atomic data used for T_e , n_e , and ionic abundance calculations in Table 2. We detect the T_e -sensitive [O III] λ 4364 and [S III] λ 6314 emission lines as well as their strong-line counterparts at high-S/N, which characterize the gas in the high- and intermediate-ionization zones, respectively. To calculate T_e from these ions, we use the [O III] λ 4364/[O III] λ 5008 and [S III] λ 6314/[S III] λ 9533 ratios (where the flux of [S III] λ 9533 has been corrected to the H β flux using the theoretical P8/H β ratio, see §2) in the PYNEB GETTEM-DEN function assuming a constant n_e of 10^2 cm $^{-3}$. We use the same function and the [S II] λ 6718,6733 doublet to calculate n_e at the measured $T_e[\text{S III}]$. The electron density, $n_e[\text{S II}]=73\pm 68$ cm $^{-3}$, is less than the average n_e measured in high- z star-forming galaxies (~ 250 cm $^{-3}$, Sanders et al. 2016; Strom et al. 2017) and is in the low-density limit where abundances derived from most optical CELs are relatively insensitive to n_e . To determine uncertainties on T_e and n_e , we generate a distribution of 500 line ratios centered on the measured ratio and with standard deviation equal to the un-

¹ The direct $I([\text{S III}])/I(\text{H}\beta)$ after scaling the G395M continuum to match the G235M continuum is 0.24 ± 0.03 ; adopting this intensity ratio results in a larger, but consistent, $T_e[\text{S III}]$ than reported in §3. Therefore, the abundance results discussed in §4.1 are qualitatively robust to the lower intensity ratio.

Table 1. D40 Line Fluxes & Intensities

G235M		
Emission Line	F(λ)/F(H β)	I(λ)/I(H β)
H γ 4342	0.420 \pm 0.026	0.451 \pm 0.031
[O III] 4364	0.081 \pm 0.007	0.087 \pm 0.008
He I 4473	0.039 \pm 0.004	0.041 \pm 0.004
He II 4687	0.016 \pm 0.003	0.016 \pm 0.003
[Ar IV] 4713	0.003 \pm 0.003	0.003 \pm 0.003
He I 4715	0.007 \pm 0.003	0.007 \pm 0.003
H β 4863	1.000 \pm 0.060	1.000 \pm 0.060
[O III] 4960	2.014 \pm 0.121	1.993 \pm 0.120
[O III] 5008	6.002 \pm 0.361	5.914 \pm 0.358
He I 5017	0.028 \pm 0.004	0.027 \pm 0.004
He I 5877	0.003 \pm 0.003	0.107 \pm 0.008
[O I] 6302	0.061 \pm 0.004	0.055 \pm 0.004
[S III] 6314	0.018 \pm 0.002	0.017 \pm 0.002
[O I] 6366	0.019 \pm 0.002	0.017 \pm 0.002
Si II 6373	0.006 \pm 0.002	0.006 \pm 0.002
[N II] 6550	0.042 \pm 0.003	0.038 \pm 0.003
H α 6565	3.051 \pm 0.183	2.760 \pm 0.208
[N II] 6585	0.112 \pm 0.007	0.101 \pm 0.008
He I 6680	0.031 \pm 0.002	0.028 \pm 0.003
[S II] 6718	0.146 \pm 0.009	0.131 \pm 0.010
[S II] 6733	0.108 \pm 0.007	0.097 \pm 0.008
He I 7067	0.034 \pm 0.003	0.030 \pm 0.003
[Ar III] 7138	0.053 \pm 0.004	0.047 \pm 0.004
[O II] 7322	0.028 \pm 0.003	0.025 \pm 0.003
[O II] 7332	0.023 \pm 0.002	0.020 \pm 0.002
F(H β) (erg/s/cm 2)	(8.65 \pm 0.03) $\times 10^{-18}$	
E(B-V)	0.12 \pm 0.05	

G395M		
Emission Line	F(λ)/F(P8)	I(λ)/I(H β)
[S III] 9071	3.037 \pm 0.302	0.109 \pm 0.011
[S III] 9533	7.980 \pm 0.774	0.286 \pm 0.028
P8 9549	1.000 \pm 0.123	0.036 \pm 0.004
P7 10053	1.899 \pm 0.204	...
He I 10833	7.894 \pm 0.769	...
P6 10941	2.360 \pm 0.246	...
P5 12822	3.543 \pm 0.352	...
F(P8) (erg/s/cm 2)	(0.32 \pm 0.02) $\times 10^{-18}$	

NOTE—Line fluxes and intensities measured from the NIRSpect rest optical and NIR data of D40. *Top:* Emission lines (Left), line flux relative to H β (Center), and reddening-corrected intensities relative to H β (Right) measured in the G235M spectrum. The last two rows provide the flux of H β and E(B-V). *Bottom:* Emission lines (Left), line flux relative to P8 (Center), and intensity ratios relative to H β using the theoretical P8/H β ratio (Right). For the G395M data, we only report the inferred $I(\lambda)/I(\text{H}\beta)$ for lines in close proximity to P8. The last row reports the measured flux of P8.

Table 2. Adopted Atomic Data

Ion	Transition Probabilities	Collision Strengths
N ⁺	Froese Fischer & Tachiev (2004)	Tayal (2011)
O ⁺	Froese Fischer & Tachiev (2004)	Kisielius et al. (2009)
O ²⁺	Froese Fischer & Tachiev (2004)	Storey et al. (2014)
S ⁺	Irimia & Froese Fischer (2005)	Tayal & Zatsarinny (2010)
S ²⁺	Froese Fischer et al. (2006)	Hudson et al. (2012)
Ar ²⁺	Mendoza & Zeippen (1983)	Munoz Burgos et al. (2009)
Ar ³⁺	Mendoza & Zeippen (1982)	Ramsbottom & Bell (1997)

certainty on the emission line ratio. We then calculate the resulting T_e or n_e distribution and take the standard deviation as the uncertainty.

Table 3 reports the physical conditions measured in D40. The direct T_e in D40, $T_e[\text{O III}] = 13200 \pm 500$ K and $T_e[\text{S III}] = 14700 \pm 1400$ K, are plotted in Figure 2 alongside T_e measurements in extragalactic H II regions (from Berg et al. 2020; Rogers et al. 2021, 2022) and low-metallicity dwarf galaxies (Berg et al. 2021; Izotov et al. 2021; Thuan et al. 2022; Arellano-Córdova et al. 2022b). The empirical T_e - T_e scaling relation of Rogers et al. (2021) and photoionization model relation of Garnett (1992) are provided as solid blue and red lines, respectively. The $T_e[\text{O III}]$ and $T_e[\text{S III}]$ measurements in D40 are in good agreement with the T_e measured in local star-forming systems and with the empirical T_e - T_e scaling relation, although there are few extragalactic H II regions with similarly high $T_e[\text{O III}]$ and $T_e[\text{S III}]$. While this relation appears to characterize the T_e in D40, we emphasize that large sample sizes are required to assess the scatter about a given T_e - T_e relation (e.g., Arellano-Córdova & Rodríguez 2020; Yates et al. 2020; Rogers et al. 2021) and whether these relations describe the bulk T_e trends at high- z .

While we detect intense $[\text{O II}]\lambda\lambda 7322, 7332$ auroral line emission in D40, we lack the nebular lines to estimate the low-ionization zone T_e directly from the NIRSPEC data. Future work will utilize ground-based $[\text{O II}]\lambda\lambda 3727, 3729$ detections to directly measure $T_e[\text{O II}]$ in the CECILIA galaxies. Given the good agreement with the empirical $T_e[\text{O III}]$ - $T_e[\text{S III}]$ relation, we infer the low-ionization zone T_e using the weighted average approach recommended by Rogers et al. (2021). First, we use the direct $T_e[\text{O III}]$ and $T_e[\text{S III}]$ to estimate the low-ionization zone temperature using Equations 3 and 6 in Rogers et al. (2021). We also apply their Equation 8 to account for the intrinsic T_e scatter about each relation when calculating the uncertainty on the inferred T_e . Next, we take the weighted average of the two inferred T_e and adopt this as $T_{e,Low}$. Finally, we use the largest inferred T_e uncertainty as the uncertainty on $T_{e,Low}$. The inferred low-

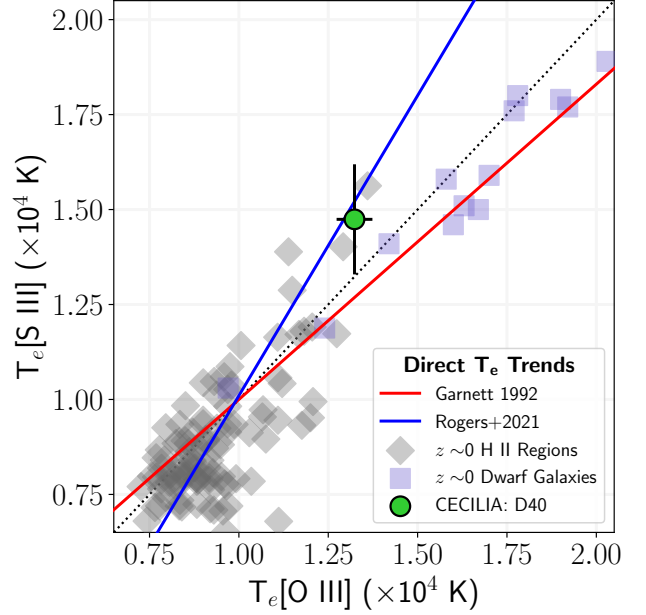


Figure 2. $T_e[\text{S III}]$ - $T_e[\text{O III}]$ trends measured in $z \sim 0$ extragalactic H II regions (gray diamonds, see §3) and dwarf galaxies (blue squares, see §3), and in D40 (green circle) at $z \sim 3$. The Garnett (1992) photoionization model $T_e[\text{S III}]$ - $T_e[\text{O III}]$ relation is shown as the solid red line; the empirical scaling relation of Rogers et al. (2021) is provided as the solid blue line. The dotted line represents equal $T_e[\text{S III}]$ and $T_e[\text{O III}]$. The T_e measured in D40 agree with the T_e trends of local ionized regions and the empirical T_e - T_e scaling relation.

ionization zone temperature, $T_{e,Low} = 12300 \pm 1000$ K, is also reported in Table 3.

3.2. Abundances and Ionization Correction Factors

We calculate ionic abundances relative to H^+ using the PYNEB GETIONABUNDANCE function, the strong-line intensities, the ionization zone T_e , and $n_e[\text{S II}]$. Uncertainty on the line intensity and emissivity ratios (the latter of which is dependent on the T_e uncertainty) are added in quadrature to calculate the ionic abundance uncertainty. Table 3 reports the direct and inferred ionic abundances measured in D40. The inferred O^+/H^+ abundance is calculated from the $[\text{O II}]$ auroral lines, which are sensitive to T_e and n_e . While some studies have found good consistency between O^+/H^+ abundances derived using the nebular and auroral $[\text{O II}]$ lines (Kniazev et al. 2003, 2004), others with direct low- and high-ionization zone T_e measure inconsistent O^+/H^+ abundances from the different $[\text{O II}]$ lines (Rodríguez 2020). Furthermore, Méndez-Delgado et al. (2023b) recently showed that n_e fluctuations have the potential to bias O^+/H^+ abundances upwards by ~ 0.1 dex when calculated using the $[\text{O II}]$ auroral lines. Such fluctuations are not explicitly accounted for here, but the relatively large O^+/H^+ uncertainty in D40 reflects the T_e -sensitivity of $[\text{O II}]\lambda\lambda 7322, 7332$ auroral lines

when used for ionic abundances. O^+ and O^{2+} are the two relevant ionic states of O in the ISM for systems ionized by O and B stars (Berg et al. 2021). While we detect intense [O I] λ 6302 emission, this emission could be reflective of the photodissociation region rather than the ionized gas. As such, we assume the total O abundance is described by $O/H \approx (O^+ + O^{2+})/H^+$. The resulting O/H abundance in D40 is $12+\log(O/H) = 8.07 \pm 0.06$ dex, $\sim 24\%$ of the solar abundance (see §4). We do not correct for dust grain depletion of O, which is most significant in high-metallicity environments (up to 0.1 dex at solar metallicity, see Peimbert & Peimbert 2010; Peña-Guerrero et al. 2012). Given the similar IP of N^+ and O^+ , we adopt the usual approximation that $N/O \approx N^+/O^+$, which is good to within 10% of the true gas-phase N/O (see Nava et al. 2006; Amayo et al. 2021).

For other elements, ionization correction factors (ICFs) are required to account for the abundances of unobserved ionic species. Given an ionic abundance X^{i+}/H^+ , the total elemental abundance X/H is calculated as $X/H = ICF(X) \times X^{i+}/H^+$ where $ICF(X)$ depends on the ionization state of the gas. For example, there are no observable [S IV] emission lines in the optical or NIR, but the missing S^{3+} must be accounted for when calculating total S abundances. Similarly, correction for Ar^+ is required for total Ar abundance, as is an additional correction for Ar^{3+} in very high-ionization systems if the optical [Ar IV] $\lambda\lambda$ 4713,4742 lines are not detected (see the discussion at the end of this section).

Owing to the challenges associated with measuring empirical total abundances, ICFs are calibrated via two methods: with similarities in IP (like N and Ne, Peimbert & Costero 1969), and with photoionization models (Thuan et al. 1995; Izotov et al. 2006; Amayo et al. 2021). The latter are required for S and Ar abundances, but these photoionization models necessarily make assumptions about the ionizing spectrum that may not describe high- z galaxies, which have generally harder ionizing spectra. For example, Amayo et al. (2021) developed ICFs from the Bayesian Oxygen and Nitrogen Determinations (Vale Asari et al. 2016) grid of models, which utilize PopStar single-star SEDs (Mollá et al. 2009) with varying gas-phase O/H and N/O. To calibrate these ICFs, Amayo et al. (2021) weighted each model based on its ability to reproduce the emission line trends of local blue compact galaxies and H II regions on the classic Baldwin-Philips-Terlevich (BPT) diagram (Baldwin et al. 1981), or $\log([O III]\lambda 5008/H\beta)$ vs. $\log([N II]\lambda 6585/H\alpha)$. It is well-established that high- z star-forming galaxies are offset from the $z \sim 0$ BPT star-forming locus (Masters et al. 2014; Steidel et al. 2014; Shapley et al. 2015; Strom et al. 2017; Sanders et al. 2023b), and it follows that these ICFs may not be suitable for high- z galaxies or other sources with harder ionizing spectra. While some studies have considered harder ioniz-

Table 3. D40 Physical Conditions

Property	Measurement
$T_e[O III]$ (K)	13200 ± 500
$T_e[S III]$ (K)	14700 ± 1400
$T_{e,Low}$ (K, inferred)	12300 ± 1000
$n_e[S II]$ (cm^{-3})	73 ± 71
$O^+/H^+ (\times 10^5)$	3.0 ± 1.3
$O^{2+}/H^+ (\times 10^5)$	8.8 ± 1.1
$12+\log(O/H)$ (dex)	8.07 ± 0.06
$N^+/H^+ (\times 10^6)$	1.3 ± 0.3
$\log(N/O)$ (dex)	-1.37 ± 0.21
$S^+/H^+ (\times 10^7)$	3.5 ± 0.7
$S^{2+}/H^+ (\times 10^7)$	8.9 ± 1.7
S ICF	1.24 ± 0.12
$12+\log(S/H)$ (dex)	6.19 ± 0.08
$\log(S/O)$ (dex)	-1.88 ± 0.10
$Ar^{2+}/H^+ (\times 10^7)$	1.7 ± 0.4
Ar ICF	1.07 ± 0.11
$12+\log(Ar/H)$ (dex)	5.27 ± 0.10
$\log(Ar/O)$ (dex)	-2.80 ± 0.12
$Ar^{3+}/H^+ (\times 10^7)_u$	1.0 ± 0.5
Ar ICF _u	1.01 ± 0.10
$\log(Ar/O)_u$ (dex)	< -2.63

NOTE— T_e , n_e , ionic abundances, ICFs, and total abundances measured in D40. We also report $(Ar^{3+}/H^+)_u$, the upper limit on Ar^{3+} abundance assuming the combined [Ar IV] λ 4713 and He I λ 4715 emission is entirely [Ar IV]. The resulting change to the ICF, Ar ICF_u, and relative abundance, $\log(Ar/O)_u$, are reported in the last two rows.

ing sources when calibrating ICFs (e.g., Berg et al. 2021), it is unclear if these can reproduce the general emission line trends of high- z galaxies.

For the present study, we use the S and Ar ICFs of Izotov et al. (2006) for abundances in D40. These ICFs are dependent on O^+/O and have different functional forms depending on $12+\log(O/H)$; as recommended by Izotov et al. (2006), we use a linear interpolation of intermediate- and high-metallicity ICFs for D40. However, we emphasize that the lack of available ICFs that are calibrated either on the strong-line trends in high- z galaxies or model grids which consider other ionizing sources (e.g., binary stars, Eldridge et al. 2017; Stanway & Eldridge 2018) presents one of the largest uncertainties when attempting to estimate the total

abundance of elements like S and Ar. To partially account for this, we assume a 10% uncertainty in applying the Izotov et al. (2006) S and Ar ICFs. In future works, we will leverage the CECILIA sample and new grids of photoionization models to derive physically-motivated ICFs for reliable total abundance inferences in high- z environments.

Finally, we note that the blend of [Ar IV] λ 4713 and He I λ 4715 is detected in D40. In high-ionization sources, the ionic fraction of Ar $^{3+}$ becomes comparable to that of Ar $^{2+}$ (e.g., Berg et al. 2021); as such, [Ar IV] emission permits a direct measurement of Ar $^{3+}/\text{H}^+$ and a total Ar/H that is less susceptible to the uncertainties of the adopted ICF (i.e., the ICF is only accounting for the missing Ar $^+/\text{H}^+$ abundance). However, the Gaussian fit to [Ar IV] λ 4713 indicates that this line is only weakly detected (S/N \sim 1). As an exercise meant to provide an upper limit on Ar/H, we attribute the [Ar IV] λ 4713 and He I λ 4715 blend entirely to [Ar IV], calculate the resulting Ar $^{3+}/\text{H}^+$ abundance using $T_e[\text{O III}]$, and determine Ar/H using (Ar $^{2+}$ + Ar $^{3+})/\text{H}^+$ and the alternative Ar ICF proposed by Izotov et al. (2006). The resulting upper limit on Ar/O is reported as $\log(\text{Ar}/\text{O})_u$ in Table 3.

4. DISCUSSION

4.1. Abundance Results

We now compare the abundance trends measured in D40 to local star-forming systems, illustrated in Figure 3. The relative abundances of N/O, S/O, or Ar/O are plotted against the gas-phase O/H abundance. The local H II regions and dwarf galaxies from Figure 2 (i.e., those with simultaneous $T_e[\text{O III}]$ and $T_e[\text{S III}]$) are represented as gray diamonds and blue squares, respectively. We denote abundances in $z \sim 0$ dwarf galaxies from Skillman et al. (2013), Berg et al. (2019), and Aver et al. (2022) that have measurements of $T_e[\text{O III}]$ but are missing $T_e[\text{S III}]$ as open blue squares. We also represent solar abundances reported in Asplund et al. (2021) as the \odot symbol and dotted orange lines (fixed solar O/H), with the shaded regions indicating the uncertainty.

The O/H abundance measured in D40, $12+\log(\text{O}/\text{H}) = 8.07 \pm 0.06$ dex, is indicative of a relatively metal-poor ISM. While this is lower than the average model-inferred metallicity of the KBSS galaxies reported in Strom et al. (2018), D40's O/H is consistent with its relatively high $T_e[\text{O III}]$ and $T_e[\text{S III}]$ and is in general agreement with emerging direct O/H abundance trends at $z > 1$ (e.g., Sanders et al. 2023a; Welch et al. 2024). In the top panel, the inferred $\log(\text{N}/\text{O})$ abundance in D40 (green circle, -1.37 ± 0.21 dex) is in good agreement with the primary N/O plateau ($\log(\text{N}/\text{O}) \sim -1.43$ dex, Garnett 1990; van Zee & Haynes 2006; Nava et al. 2006) established by high-ionization, low-metallicity dwarf galaxies and H II regions. The metallicity of D40 is close to the $12+\log(\text{O}/\text{H})$ value where secondary N production from intermediate-mass stars is expected to become significant

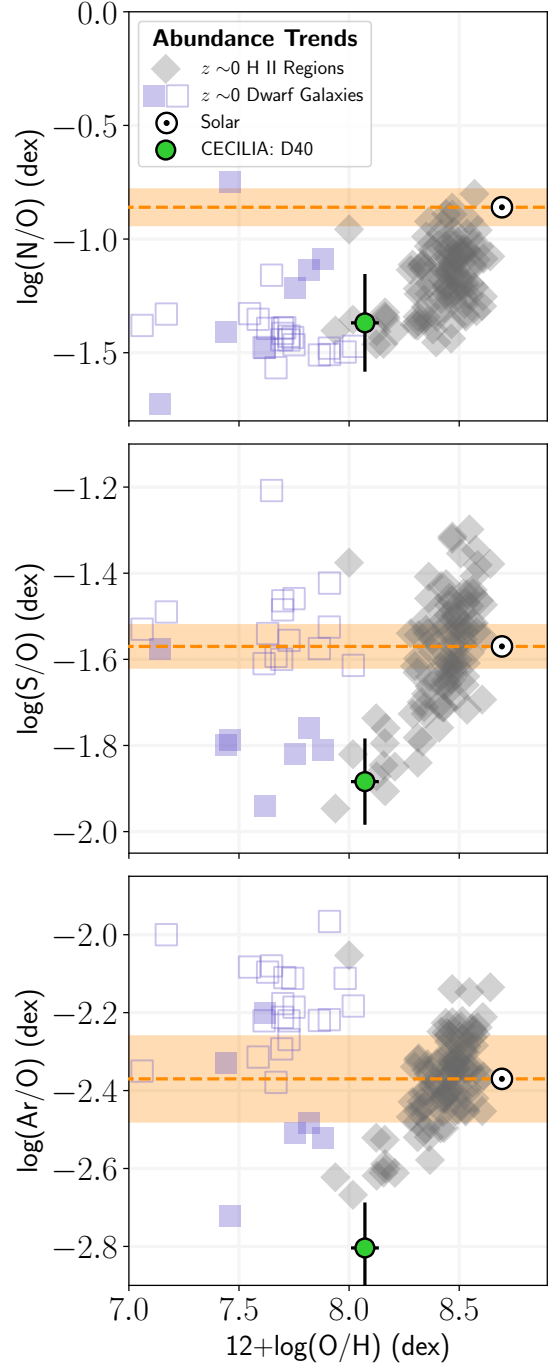


Figure 3. Abundance trends of D40 (green circle), local H II regions (gray diamonds), and low-metallicity dwarf galaxies (blue squares). Open blue squares represent dwarf galaxies without direct $T_e[\text{S III}]$. The \odot denotes solar abundances from Asplund et al. (2021); the dashed orange line and shaded areas are the solar N/O, S/O, and Ar/O ratios. *Top Panel:* $\log(\text{N}/\text{O})$ vs. $12+\log(\text{O}/\text{H})$. *Middle Panel:* $\log(\text{S}/\text{O})$ vs. $12+\log(\text{O}/\text{H})$. *Bottom Panel:* $\log(\text{Ar}/\text{O})$ vs. $12+\log(\text{O}/\text{H})$. The first T_e -based S and Ar abundances at $z \sim 3$ indicate sub-solar S/O and Ar/O, suggesting that these three elements are sensitive to O/H or star-formation history.

($12+\log(\text{O}/\text{H}) \sim 8.3$ dex, see Henry et al. 2000), but given that we do not observe enhanced N/O, the N enrichment in D40 likely arises from primary nucleosynthesis from massive stars. We note that the large uncertainty on the $\log(\text{N}/\text{O})$ relative abundance is related to the dependence of N^+ and O^+ on the inferred low-ionization zone T_e and the use of the [O II] auroral lines for O^+ abundance.

O, S, and Ar are all generally thought to be primarily produced by the α process in massive stars and are released to the ISM on relatively short timescales via CCSN. In this scenario, the relative abundances of S/O and Ar/O are related to CCSN yields and independent of metallicity. Therefore, it is of interest to assess any potential metallicity or redshift evolution of relative α abundances, which would suggest alternative enrichment mechanisms for the different elements. The inferred gas-phase S/O abundance measured in D40, $\log(\text{S}/\text{O}) = -1.88 \pm 0.10$ dex, is 2σ below the solar abundance ratio² but is consistent with the lowest S/O abundances reported in local ionized regions. The average S/O observed in the local objects, $\langle \log(\text{S}/\text{O})_{z=0} \rangle = -1.58 \pm 0.14$ dex, shows relatively large dispersion, which might be related to the challenges associated with observing the [S III] $\lambda\lambda 9071, 9533$ lines from ground-based observatories. For example, contamination from telluric absorption features (Noll et al. 2012) can bias the NIR [S III] emission line intensities low and the derived $T_e[\text{S III}]$ high, resulting in large dispersion in S/H and S/O. Telluric contamination, however, does not affect our JWST/NIRSpec observations of D40's [S III] lines or S/O abundance, the latter of which is consistent with the S/O of H II regions with similarly low $12+\log(\text{O}/\text{H})$. Taken together with the S/O abundances in dwarf galaxies with measured $T_e[\text{S III}]$, there is tentative evidence for a more complex enrichment mechanism for S that leads to deviations from the abundance patterns expected from CCSN enrichment alone.

The bottom panel of Figure 3 reveals that the inferred relative Ar/O abundance in D40, $\log(\text{Ar}/\text{O}) = -2.80 \pm 0.12$ dex, is also significantly sub-solar. The same conclusion is reached when considering the upper limit of Ar/O from the maximum [Ar IV] intensity, $\log(\text{Ar}/\text{O})_u < -2.63$ dex. Other available Ar ICFs produce similarly low Ar/O, with the maximum $\log(\text{Ar}/\text{O})$ being -2.60 dex when using the Thuan et al. (1995) ICFs. Furthermore, accounting for the depletion of metals onto dust grains would increase the O abundance and only further decrease Ar/O. The average $\log(\text{Ar}/\text{O})$ for the $z \sim 0$ SF systems is $\langle \log(\text{Ar}/\text{O})_{z=0} \rangle = -2.38 \pm 0.15$ dex, in agreement with the Asplund et al. (2021) solar ratio. Both $\langle \log(\text{Ar}/\text{O})_{z=0} \rangle$ and the solar Ar/O are larger than the gas-phase $\log(\text{Ar}/\text{O})$ in D40 by $>2\sigma$.

To further explore these abundance trends, we investigate the relative Ar/S abundance in D40. The $\log(\text{Ar}/\text{S})$ abundance measured when using the inferred total S/H and Ar/H abundances reported in Table 3 is $\log(\text{Ar}/\text{S}) = -0.92 \pm 0.13$ dex. While this is below the solar abundance ratio of $\log(\text{Ar}/\text{S})_{\odot} = -0.74 \pm 0.10$ dex, it is also sensitive to the shortcomings in the adopted S and Ar ICFs. For example, if we instead consider the maximum Ar abundance from the upper limit on $\text{Ar}^{3+}/\text{H}^+$, we find $\log(\text{Ar}/\text{S})_u < -0.76$ dex, which agrees with the solar ratio. Even this upper limit is sensitive to the aforementioned shortcomings of the ICFs, which may fail to account for a significant fraction of S^{3+} and Ar^+ in the ISM. Given the similar IPs of S^+ (23.3 eV) and Ar^+ (27.6 eV), $\log(\text{Ar}^{2+}/\text{S}^{2+})$ has been proposed as an alternative, ICF-independent measure of $\log(\text{Ar}/\text{S})$ (Kennicutt et al. 2003; Croxall et al. 2016). For D40, we measure a direct $\log(\text{Ar}^{2+}/\text{S}^{2+}) = -0.71 \pm 0.12$ dex, in good agreement with the solar $\log(\text{Ar}/\text{S})$ ratio. Taken together with the abundance trends from Figure 3, the ISM in D40 at $z \sim 3$ is S and Ar deficient relative to O when compared to the gas-phase abundances in the local universe, yet the relative Ar/S abundance at high- z and in local objects is consistent with a joint evolution of Ar and S.

4.2. S/O, Ar/O, and Implications for α Enhancement

While it is often assumed that the relative α element abundance ratios are independent of $12+\log(\text{O}/\text{H})$, ionization, or star-formation history, recent nucleosynthesis models have revealed that Type Ia SNe can produce certain α elements. For example, the models of Kobayashi et al. (2020a,b) indicate that the relative yields of $^{32}\text{S}/^{56}\text{Fe}$ and $^{36}\text{Ar}/^{56}\text{Fe}$ from different Type Ia progenitors can match the observed solar S/Fe and Ar/Fe abundance ratios, respectively. Furthermore, these models indicate that the Type Ia SNe yield of S and Ar are roughly the same and significantly greater than the yield of O in different Type Ia progenitors (see Kobayashi et al. 2020b). This suggests that the relative abundances of α elements like S/O and Ar/O trace enrichment by both CCSN and Type Ia SNe in a manner similar to Fe/O. Indeed, galactic chemical evolution models can match the Ar/O and Ar/H abundances of stars and planetary nebulae in M31 using various star-formation histories to account for the different mechanisms of Ar production (Arnaboldi et al. 2022; Kobayashi et al. 2023).

In this scenario, rapid enrichment from CCSN results in enhanced O relative to S and Ar, producing lower gas-phase $\log(\text{S}/\text{O})$ and $\log(\text{Ar}/\text{O})$ abundance ratios. Type Ia SNe enrich the ISM with additional S and Ar, thereby increasing $\log(\text{S}/\text{O})$ and $\log(\text{Ar}/\text{O})$ after a large time delay (from ~ 0.1 to > 10 Gyr, Kobayashi & Nomoto 2009; Kobayashi et al. 2020b). Unlike the $\log(\text{S}/\text{O})$ and $\log(\text{Ar}/\text{O})$ abundance ratios, the $\log(\text{Ar}/\text{S})$ abundance should remain relatively con-

² We emphasize that the reported uncertainties on S/O and Ar/O do not reflect systematic errors related to the ICFs, which may have different functional forms in high- z galaxies (see discussion in §3.2).

stant (consistent with direct abundance trends in the local universe, [Stevenson et al. 1993](#)) if the enrichment of these elements is set by CCSN at early times and if the yield of S and Ar are similar for Type Ia SNe at late times ([Kobayashi et al. 2020b](#)). The lifetime of the massive stars ionizing the ISM is much shorter than the Type Ia SNe time delay, such that the chemical compositions of the H II regions are reflective of the stars that were born in this environment. Considering this time delay and the age of the Universe at D40’s redshift (~ 2 Gyr for $z=2.9628$), the S/O and Ar/O abundance trends in D40 could be explained by predominant enrichment from CCSN that results in enhanced gas-phase O relative to S and Ar.

The S and Ar abundance trends presented here are the first to be directly calculated from a measured $T_e[\text{S III}]$ and strong lines of [S III] and [Ar III] in a galaxy at $z>0.2$. Currently, no prior observations have constrained $T_e[\text{S III}]$ in high- z galaxies, which is necessary for reliable S/O and Ar/O abundances. Additionally, the [S III] and [Ar III] strong lines require both broad wavelength coverage and fairly deep integration times to detect. For example, [Isobe et al. \(2023\)](#) only detect [Ar III] $\lambda 7138$ in two galaxies at $z>4$, but $T_e[\text{O III}]$ and $T_e[\text{S III}]$ are unconstrained in both galaxies and all other Ar abundances are upper limits. Furthermore, the S/O abundances from [Isobe et al. \(2023\)](#) are determined using the [S II] emission lines alone, which accounts for only a small fraction of the total S abundance in high-ionization galaxies. For example, the S^{2+}/H^+ abundance in D40 is >2.5 times that of S^+/H^+ (see Table 3), implying that a measure of only S^+/H^+ is heavily reliant on the validity of the S ICF applied (which we note is one of the largest uncertainties related to high- z abundance inferences, see discussion in §3.2).

If these first constraints on the gas-phase S/O and Ar/O abundance trends at high- z are the result of primary enrichment from CCSN, then these data add to the growing observational evidence of a disconnect between the nucleosynthesis products of Type II and Ia SNe in the early universe. As mentioned in §3.2, the emission line ratios of high- z star-forming galaxies are offset in the BPT diagram, a trend that can be explained with a harder ionizing spectrum at fixed O/H ([Steidel et al. 2014](#); [Strom et al. 2017](#); [Sanders et al. 2020](#); [Topping et al. 2020](#); [Runco et al. 2021](#)). By decoupling the stellar and nebular metallicities in photoionization models, [Strom et al. \(2018\)](#) demonstrated that the bulk emission line trends of $z>2$ galaxies can be reproduced with lower stellar metallicity (to reduce the line-blanketing by Fe lines) relative to the nebular metallicity (which influences the strong optical emission lines such as [O III] $\lambda 5008$). Stacks of rest-UV spectra of high- z star-forming galaxies arrive at similar conclusions: spectral synthesis of low-metallicity stellar populations is required to match the UV features which are dominated by Fe, but larger gas-phase O abundance is needed to

produce the observed strong line ratios (e.g., [Steidel et al. 2016](#); [Cullen et al. 2019](#); [Topping et al. 2020](#)). A pattern of sub-solar S/O and Ar/O relative abundances with simultaneous solar Ar/S abundance ratios at high- z would suggest that the differences in enrichment timescales play a crucial role in the gas-phase conditions observed in early star-forming galaxies. Utilizing S/O and Ar/O as tracers of Type Ia SNe and O/H as a tracer of CCSN enrichment has the additional benefit that the required CELs are entirely observable in the rest-frame optical/NIR. Therefore, the [Ar III] $\lambda 7138$ emission line may act as an accessible tracer of these different enrichment mechanisms, providing further insight into chemical enrichment histories of high- z galaxies.

5. CONCLUSIONS

We report the chemical abundance trends in Q2343-D40, a galaxy at $z=2.9628\pm 0.0001$ observed with JWST/NIRSpec as part of the CECILIA program. For the first time in a galaxy at $z>0.2$, we calculate $T_e[\text{S III}]$ from the [S III] $\lambda 6314$ auroral line and the [S III] $\lambda 9533$ strong line. We utilize the high-S/N detections of [O III] $\lambda 4364$ and [O III] $\lambda 5008$ to directly calculate the high-ionization zone T_e . The T_e trends in D40, $T_e[\text{O III}]=13200\pm 500$ K and $T_e[\text{S III}]=14700\pm 1400$ K, are in good agreement with the [Rogers et al. \(2021\)](#) empirical T_e - T_e relation (see Figure 2), but we note that other surveys have found large scatter in $T_e[\text{S III}]$ at fixed $T_e[\text{O III}]$. While $T_e[\text{S III}]$ is challenging to measure, owing to the broad wavelength coverage required to measure [S III] $\lambda\lambda 9071, 9533$ and the low intensity of the [S III] auroral line, simultaneous measurements of $T_e[\text{S III}]$ and $T_e[\text{O III}]$ are required to assess whether T_e - T_e scaling relations calibrated on local ionized nebulae or photoionization models are appropriate to apply at high- z .

We use these direct $T_e[\text{O III}]$ and $T_e[\text{S III}]$ values to measure the gas-phase ionic abundances in D40, representing the first direct abundances of S^{2+}/H^+ and $\text{Ar}^{2+}/\text{H}^+$ in a high- z galaxy. Using an inferred low-ionization zone T_e and the necessary ICFs, we calculate the inferred total O/H abundance and the relative abundances of N/O, S/O, and Ar/O (plotted in Figure 3). The O/H abundance in D40, $12+\log(\text{O}/\text{H}) = 8.07 \pm 0.06$, is $\sim 24\%$ solar, and the N/O abundance agrees with the primary N/O plateau observed in similarly metal-poor galaxies in the local universe. The relative S/O abundance in D40 is below the solar abundance ratio by more than 2σ (0.31 dex), but is in agreement with the lowest S/O abundances observed in local star-forming regions. The S/O abundance dispersion in local ionized regions is possibly related to the observational challenges associated with measuring the NIR [S III] lines from the ground. Alternatively, the scatter in S/O may be related to the ICFs, which must account for a large fraction of unobserved S^{3+} in regions characterized by high-ionization.

The Ar/O abundance in D40, $\log(\text{Ar}/\text{O}) = -2.80 \pm 0.12$ dex, is $>2\sigma$ (0.43 dex) below the solar abundance ratio and the average $\log(\text{Ar}/\text{O})$ observed in $z \sim 0$ star-forming systems. This result is robust to the inclusion of Ar^{3+} from the maximum possible $[\text{Ar IV}]\lambda 4713$ intensity, reddening correction uncertainties, and the effects of dust depletion. While the inferred S/O abundance is sensitive to the functional form of the ICF, a systematic error with the ICF is less likely to alter the estimated maximum Ar/O because such a scenario would imply a significant fraction of missing Ar^+ in the high-ionization ISM of D40. Comparing the direct Ar^{2+} and S^{2+} abundances in D40, we measure $\log(\text{Ar}^{2+}/\text{S}^{2+}) \approx \log(\text{Ar}/\text{S}) = -0.71 \pm 0.12$ dex, in good agreement with the solar Ar/S abundance.

Modern nucleosynthesis models find that S and Ar are produced via the α process in massive stars and in Type Ia SNe (Kobayashi et al. 2020a,b). In this way, S/O and Ar/O are sensitive to the relative contributions from Type II and Ia SNe. Additionally, the yield of S and Ar are similar for different Type Ia progenitor models, implying that the Ar/S ratio remains relatively constant from both CCSN and Type Ia enrichment. As such, the inferred sub-solar S/O and Ar/O abundances, coupled with the Ar/S ratio that matches the solar value, could be the result of primarily CCSN enrichment with small contributions from Type Ia SNe, an indirect probe of the relative enrichment of O with respect to Fe.

If future JWST observations and more secure ICFs confirm that low S/O and Ar/O abundances are common in high- z galaxies, then such abundance trends would corroborate the growing evidence of enhanced O relative to the nucleosynthesis products of Type Ia SNe, including the hard ionizing spectra required to reproduce the BPT offset and the inferred stellar abundances measured from stacked rest-frame UV spectra of high- z galaxies. Abundances like N/O, S/O, and Ar/O provide another route to explore these relative en-

richment pathways and the physical conditions within these systems. With deep rest-frame UV, optical, and NIR spectra of many $z > 2$ star-forming galaxies, the CECILIA sample is poised to address these relative abundance trends in the early universe where the timescales of Type II and Ia SNe enrichment play an important role.

We are grateful to the referee for their constructive review of the manuscript and their insightful recommendations. N.S.J.R. is supported under JWST-GO-02593, which was provided by NASA through a grant from the Space Telescope Science Institute, which is operated by the Association of Universities for Research in Astronomy, Inc., under NASA contract NAS 5-03127. A.L.S., G.C.R., and R.F.T. acknowledge partial support from the JWST-GO-02593.008-A, JWST-GO-02593.004-A, and JWST-GO-02593.006-A grants, respectively. R.F.T. also acknowledges support from the Pittsburgh Foundation (grant ID UN2021-121482) and the Research Corporation for Scientific Advancement (Cottrell Scholar Award, grant ID 28289).

This work is primarily based on observations made with NASA/ESA/CSA JWST, associated with PID 2593, which can be accessed via doi: [10.17909/x66z-p144](https://doi.org/10.17909/x66z-p144). The data were obtained from the Mikulski Archive for Space Telescopes (MAST) at the Space Telescope Science Institute, which is operated by the Association of Universities for Research in Astronomy, Inc., under NASA contract NAS 5-03127 for JWST.

Facilities: JWST (NIRSpec)

Software: MATPLOTLIB (Hunter 2007), NUMPY (Harris et al. 2020), PYNEB (Luridiana et al. 2012, 2015), SCIPY (Virtanen et al. 2020), CALWEBB (Bushouse et al. 2023), GRIZLI (Brammer 2023), MSAEXP (Brammer 2022), NSCLEAN (Rauscher 2023).

REFERENCES

- Amayo, A., Delgado-Inglada, G., & Stasińska, G. 2021, MNRAS, 505, 2361, doi: [10.1093/mnras/stab1467](https://doi.org/10.1093/mnras/stab1467)
- Arellano-Córdova, K. Z., Esteban, C., García-Rojas, J., & Méndez-Delgado, J. E. 2020, MNRAS, 496, 1051, doi: [10.1093/mnras/staa1523](https://doi.org/10.1093/mnras/staa1523)
- Arellano-Córdova, K. Z., & Rodríguez, M. 2020, MNRAS, 497, 672, doi: [10.1093/mnras/staa1759](https://doi.org/10.1093/mnras/staa1759)
- Arellano-Córdova, K. Z., Berg, D. A., Chisholm, J., et al. 2022a, ApJL, 940, L23, doi: [10.3847/2041-8213/ac9ab2](https://doi.org/10.3847/2041-8213/ac9ab2)
- Arellano-Córdova, K. Z., Mingozi, M., Berg, D. A., et al. 2022b, ApJ, 935, 74, doi: [10.3847/1538-4357/ac7854](https://doi.org/10.3847/1538-4357/ac7854)
- Arnaboldi, M., Bhattacharya, S., Gerhard, O., et al. 2022, A&A, 666, A109, doi: [10.1051/0004-6361/202244258](https://doi.org/10.1051/0004-6361/202244258)
- Arrabal Haro, P., Dickinson, M., Finkelstein, S. L., et al. 2023, ApJL, 951, L22, doi: [10.3847/2041-8213/acdd54](https://doi.org/10.3847/2041-8213/acdd54)
- Asplund, M., Amarsi, A. M., & Grevesse, N. 2021, A&A, 653, A141, doi: [10.1051/0004-6361/202140445](https://doi.org/10.1051/0004-6361/202140445)
- Aver, E., Berg, D. A., Hirschauer, A. S., et al. 2022, MNRAS, 510, 373, doi: [10.1093/mnras/stab3226](https://doi.org/10.1093/mnras/stab3226)
- Baldwin, J. A., Phillips, M. M., & Terlevich, R. 1981, PASP, 93, 5, doi: [10.1086/130766](https://doi.org/10.1086/130766)
- Berg, D. A., Chisholm, J., Erb, D. K., et al. 2021, ApJ, 922, 170, doi: [10.3847/1538-4357/ac141b](https://doi.org/10.3847/1538-4357/ac141b)
- Berg, D. A., Erb, D. K., Henry, R. B. C., Skillman, E. D., & McQuinn, K. B. W. 2019, ApJ, 874, 93, doi: [10.3847/1538-4357/ab020a](https://doi.org/10.3847/1538-4357/ab020a)

- Berg, D. A., Pogge, R. W., Skillman, E. D., et al. 2020, *ApJ*, 893, 96, doi: [10.3847/1538-4357/ab7eab](https://doi.org/10.3847/1538-4357/ab7eab)
- Berg, D. A., Skillman, E. D., Croxall, K. V., et al. 2015, *ApJ*, 806, 16, doi: [10.1088/0004-637X/806/1/16](https://doi.org/10.1088/0004-637X/806/1/16)
- Berg, D. A., Skillman, E. D., Garnett, D. R., et al. 2013, *ApJ*, 775, 128, doi: [10.1088/0004-637X/775/2/128](https://doi.org/10.1088/0004-637X/775/2/128)
- Brammer, G. 2022, msaexp: NIRSpec analysis tools, 0.3.4, Zenodo, Zenodo, doi: [10.5281/zenodo.7313329](https://doi.org/10.5281/zenodo.7313329)
- . 2023, grizli, 1.9.11, Zenodo, Zenodo, doi: [10.5281/zenodo.1146904](https://doi.org/10.5281/zenodo.1146904)
- Bresolin, F. 2011, *ApJ*, 730, 129, doi: [10.1088/0004-637X/730/2/129](https://doi.org/10.1088/0004-637X/730/2/129)
- Bunker, A. J., Saxena, A., Cameron, A. J., et al. 2023, *A&A*, 677, A88, doi: [10.1051/0004-6361/202346159](https://doi.org/10.1051/0004-6361/202346159)
- Bushouse, H., Eisenhamer, J., Dencheva, N., et al. 2023, JWST Calibration Pipeline, 1.12.5, Zenodo, doi: [10.5281/zenodo.10022973](https://doi.org/10.5281/zenodo.10022973)
- Cardelli, J. A., Clayton, G. C., & Mathis, J. S. 1989, *ApJ*, 345, 245, doi: [10.1086/167900](https://doi.org/10.1086/167900)
- Citro, A., Berg, D. A., Erb, D. K., et al. 2023, arXiv e-prints, arXiv:2305.14414, doi: [10.48550/arXiv.2305.14414](https://doi.org/10.48550/arXiv.2305.14414)
- Clarke, L., Shapley, A., Sanders, R. L., et al. 2023, *ApJ*, 957, 81, doi: [10.3847/1538-4357/acfedb](https://doi.org/10.3847/1538-4357/acfedb)
- Croxall, K. V., Pogge, R. W., Berg, D. A., Skillman, E. D., & Moustakas, J. 2016, *ApJ*, 830, 4, doi: [10.3847/0004-637X/830/1/4](https://doi.org/10.3847/0004-637X/830/1/4)
- Cullen, F., McLure, R. J., Dunlop, J. S., et al. 2019, *MNRAS*, 487, 2038, doi: [10.1093/mnras/stz1402](https://doi.org/10.1093/mnras/stz1402)
- Dinerstein, H. L. 1990, in *Astrophysics and Space Science Library*, Vol. 161, *The Interstellar Medium in Galaxies*, ed. J. Thronson, Harley A. & J. M. Shull, 257–285, doi: [10.1007/978-94-009-0595-5_10](https://doi.org/10.1007/978-94-009-0595-5_10)
- Dors, O. L., Valardi, M., Riffel, R. A., et al. 2023, *MNRAS*, 521, 1969, doi: [10.1093/mnras/stad635](https://doi.org/10.1093/mnras/stad635)
- Eldridge, J. J., Stanway, E. R., Xiao, L., et al. 2017, *PASA*, 34, e058, doi: [10.1017/pasa.2017.51](https://doi.org/10.1017/pasa.2017.51)
- Erb, D. K., Shapley, A. E., Pettini, M., et al. 2006, *ApJ*, 644, 813, doi: [10.1086/503623](https://doi.org/10.1086/503623)
- Esteban, C., Peimbert, M., García-Rojas, J., et al. 2004, *MNRAS*, 355, 229, doi: [10.1111/j.1365-2966.2004.08313.x](https://doi.org/10.1111/j.1365-2966.2004.08313.x)
- Froese Fischer, C., & Tachiev, G. 2004, *Atomic Data and Nuclear Data Tables*, 87, 1, doi: [10.1016/j.adt.2004.02.001](https://doi.org/10.1016/j.adt.2004.02.001)
- Froese Fischer, C., Tachiev, G., & Irimia, A. 2006, *Atomic Data and Nuclear Data Tables*, 92, 607, doi: [10.1016/j.adt.2006.03.001](https://doi.org/10.1016/j.adt.2006.03.001)
- Garnett, D. R. 1990, *ApJ*, 363, 142, doi: [10.1086/169324](https://doi.org/10.1086/169324)
- . 1992, *AJ*, 103, 1330, doi: [10.1086/116146](https://doi.org/10.1086/116146)
- Green, G. M. 2018, *The Journal of Open Source Software*, 3, 695, doi: [10.21105/joss.00695](https://doi.org/10.21105/joss.00695)
- Harris, C. R., Millman, K. J., van der Walt, S. J., et al. 2020, *Nature*, 585, 357, doi: [10.1038/s41586-020-2649-2](https://doi.org/10.1038/s41586-020-2649-2)
- Henry, R. B. C., Edmunds, M. G., & Köppen, J. 2000, *ApJ*, 541, 660, doi: [10.1086/309471](https://doi.org/10.1086/309471)
- Hudson, C. E., Ramsbottom, C. A., & Scott, M. P. 2012, *ApJ*, 750, 65, doi: [10.1088/0004-637X/750/1/65](https://doi.org/10.1088/0004-637X/750/1/65)
- Hunter, J. D. 2007, *Computing in Science and Engineering*, 9, 90, doi: [10.1109/MCSE.2007.55](https://doi.org/10.1109/MCSE.2007.55)
- Irimia, A., & Froese Fischer, C. 2005, *PhyS*, 71, 172, doi: [10.1238/Physica.Regular.071a00172](https://doi.org/10.1238/Physica.Regular.071a00172)
- Isobe, Y., Ouchi, M., Tominaga, N., et al. 2023, *ApJ*, 959, 100, doi: [10.3847/1538-4357/ad09be](https://doi.org/10.3847/1538-4357/ad09be)
- Izotov, Y. I., Stasińska, G., Meynet, G., Guseva, N. G., & Thuan, T. X. 2006, *A&A*, 448, 955, doi: [10.1051/0004-6361:20053763](https://doi.org/10.1051/0004-6361:20053763)
- Izotov, Y. I., Thuan, T. X., & Guseva, N. G. 2021, *MNRAS*, 508, 2556, doi: [10.1093/mnras/stab2798](https://doi.org/10.1093/mnras/stab2798)
- James, B. L., Pettini, M., Christensen, L., et al. 2014, *MNRAS*, 440, 1794, doi: [10.1093/mnras/stu287](https://doi.org/10.1093/mnras/stu287)
- Kennicutt, Robert C., J., Bresolin, F., & Garnett, D. R. 2003, *ApJ*, 591, 801, doi: [10.1086/375398](https://doi.org/10.1086/375398)
- Kisielius, R., Storey, P. J., Ferland, G. J., & Keenan, F. P. 2009, *MNRAS*, 397, 903, doi: [10.1111/j.1365-2966.2009.14989.x](https://doi.org/10.1111/j.1365-2966.2009.14989.x)
- Kniazev, A. Y., Grebel, E. K., Hao, L., et al. 2003, *ApJL*, 593, L73, doi: [10.1086/378259](https://doi.org/10.1086/378259)
- Kniazev, A. Y., Pustilnik, S. A., Grebel, E. K., Lee, H., & Pramskij, A. G. 2004, *ApJS*, 153, 429, doi: [10.1086/421519](https://doi.org/10.1086/421519)
- Kobayashi, C., Bhattacharya, S., Arnaboldi, M., & Gerhard, O. 2023, *ApJL*, 956, L14, doi: [10.3847/2041-8213/acf7c7](https://doi.org/10.3847/2041-8213/acf7c7)
- Kobayashi, C., Karakas, A. I., & Lugaro, M. 2020a, *ApJ*, 900, 179, doi: [10.3847/1538-4357/abae65](https://doi.org/10.3847/1538-4357/abae65)
- Kobayashi, C., Leung, S.-C., & Nomoto, K. 2020b, *ApJ*, 895, 138, doi: [10.3847/1538-4357/ab8e44](https://doi.org/10.3847/1538-4357/ab8e44)
- Kobayashi, C., & Nomoto, K. 2009, *ApJ*, 707, 1466, doi: [10.1088/0004-637X/707/2/1466](https://doi.org/10.1088/0004-637X/707/2/1466)
- Kriek, M., Shapley, A. E., Reddy, N. A., et al. 2015, *ApJS*, 218, 15, doi: [10.1088/0067-0049/218/2/15](https://doi.org/10.1088/0067-0049/218/2/15)
- Laseter, I. H., Maseda, M. V., Curti, M., et al. 2023, arXiv e-prints, arXiv:2306.03120, doi: [10.48550/arXiv.2306.03120](https://doi.org/10.48550/arXiv.2306.03120)
- Lequeux, J., Peimbert, M., Rayo, J. F., Serrano, A., & Torres-Peimbert, S. 1979, *A&A*, 500, 145
- Luridiana, V., Morisset, C., & Shaw, R. A. 2012, *IAU Symposium*, 283, 422, doi: [10.1017/S1743921312011738](https://doi.org/10.1017/S1743921312011738)
- . 2015, *A&A*, 573, A42, doi: [10.1051/0004-6361/201323152](https://doi.org/10.1051/0004-6361/201323152)
- Markov, V., Gallerani, S., Ferrara, A., et al. 2024, arXiv e-prints, arXiv:2402.05996, doi: [10.48550/arXiv.2402.05996](https://doi.org/10.48550/arXiv.2402.05996)
- Masters, D., McCarthy, P., Siana, B., et al. 2014, *ApJ*, 785, 153, doi: [10.1088/0004-637X/785/2/153](https://doi.org/10.1088/0004-637X/785/2/153)
- Méndez-Delgado, J. E., Esteban, C., García-Rojas, J., Kreckel, K., & Peimbert, M. 2023a, *Nature*, 618, 249, doi: [10.1038/s41586-023-05956-2](https://doi.org/10.1038/s41586-023-05956-2)

- Méndez-Delgado, J. E., Esteban, C., García-Rojas, J., et al. 2023b, *MNRAS*, 523, 2952, doi: [10.1093/mnras/stad1569](https://doi.org/10.1093/mnras/stad1569)
- Mendoza, C., & Zeppen, C. J. 1982, *MNRAS*, 198, 127, doi: [10.1093/mnras/198.1.127](https://doi.org/10.1093/mnras/198.1.127)
- . 1983, *MNRAS*, 202, 981, doi: [10.1093/mnras/202.4.981](https://doi.org/10.1093/mnras/202.4.981)
- Mollá, M., García-Vargas, M. L., & Bressan, A. 2009, *MNRAS*, 398, 451, doi: [10.1111/j.1365-2966.2009.15160.x](https://doi.org/10.1111/j.1365-2966.2009.15160.x)
- Munoz Burgos, J. M., Loch, S. D., Ballance, C. P., & Boivin, R. F. 2009, *A&A*, 500, 1253, doi: [10.1051/0004-6361/200911743](https://doi.org/10.1051/0004-6361/200911743)
- Nakajima, K., Ouchi, M., Isobe, Y., et al. 2023, arXiv e-prints, arXiv:2301.12825, doi: [10.48550/arXiv.2301.12825](https://doi.org/10.48550/arXiv.2301.12825)
- Nava, A., Casebeer, D., Henry, R. B. C., & Jevremovic, D. 2006, *ApJ*, 645, 1076, doi: [10.1086/504416](https://doi.org/10.1086/504416)
- Noll, S., Kausch, W., Barden, M., et al. 2012, *A&A*, 543, A92, doi: [10.1051/0004-6361/201219040](https://doi.org/10.1051/0004-6361/201219040)
- Peña-Guerrero, M. A., Peimbert, A., & Peimbert, M. 2012, *ApJL*, 756, L14, doi: [10.1088/2041-8205/756/1/L14](https://doi.org/10.1088/2041-8205/756/1/L14)
- Peimbert, A., & Peimbert, M. 2010, *ApJ*, 724, 791, doi: [10.1088/0004-637X/724/1/791](https://doi.org/10.1088/0004-637X/724/1/791)
- Peimbert, M. 1967, *ApJ*, 150, 825, doi: [10.1086/149385](https://doi.org/10.1086/149385)
- Peimbert, M., & Costero, R. 1969, *Boletín de los Observatorios Tonantzintla y Tacubaya*, 5, 3
- Ramsbottom, C. A., & Bell, K. L. 1997, *Atomic Data and Nuclear Data Tables*, 66, 65, doi: [10.1006/adnd.1997.0741](https://doi.org/10.1006/adnd.1997.0741)
- Rauscher, B. J. 2023, arXiv e-prints, arXiv:2306.03250, doi: [10.48550/arXiv.2306.03250](https://doi.org/10.48550/arXiv.2306.03250)
- Reddy, N. A., Shapley, A. E., Kriek, M., et al. 2020, *ApJ*, 902, 123, doi: [10.3847/1538-4357/abb674](https://doi.org/10.3847/1538-4357/abb674)
- Rodríguez, M. 2020, *MNRAS*, 495, 1016, doi: [10.1093/mnras/staa1286](https://doi.org/10.1093/mnras/staa1286)
- Rogers, N. S. J., Skillman, E. D., Pogge, R. W., et al. 2022, *ApJ*, 939, 44, doi: [10.3847/1538-4357/ac947d](https://doi.org/10.3847/1538-4357/ac947d)
- . 2021, *ApJ*, 915, 21, doi: [10.3847/1538-4357/abf8b9](https://doi.org/10.3847/1538-4357/abf8b9)
- Roy, J. R., & Kunth, D. 1995, *A&A*, 294, 432, <https://arxiv.org/abs/astro-ph/9410023>
- Rubin, R. H. 1989, *ApJS*, 69, 897, doi: [10.1086/191330](https://doi.org/10.1086/191330)
- Rudie, G. C., Steidel, C. C., Trainor, R. F., et al. 2012, *ApJ*, 750, 67, doi: [10.1088/0004-637X/750/1/67](https://doi.org/10.1088/0004-637X/750/1/67)
- Runco, J. N., Shapley, A. E., Sanders, R. L., et al. 2021, *MNRAS*, 502, 2600, doi: [10.1093/mnras/stab119](https://doi.org/10.1093/mnras/stab119)
- Sanders, R. L., Shapley, A. E., Topping, M. W., Reddy, N. A., & Brammer, G. B. 2023a, arXiv e-prints, arXiv:2303.08149, doi: [10.48550/arXiv.2303.08149](https://doi.org/10.48550/arXiv.2303.08149)
- . 2023b, *ApJ*, 955, 54, doi: [10.3847/1538-4357/acedad](https://doi.org/10.3847/1538-4357/acedad)
- Sanders, R. L., Shapley, A. E., Kriek, M., et al. 2016, *ApJ*, 816, 23, doi: [10.3847/0004-637X/816/1/23](https://doi.org/10.3847/0004-637X/816/1/23)
- Sanders, R. L., Shapley, A. E., Reddy, N. A., et al. 2020, *MNRAS*, 491, 1427, doi: [10.1093/mnras/stz3032](https://doi.org/10.1093/mnras/stz3032)
- Schaerer, D., Marques-Chaves, R., Barrufet, L., et al. 2022, *A&A*, 665, L4, doi: [10.1051/0004-6361/202244556](https://doi.org/10.1051/0004-6361/202244556)
- Schlegel, D. J., Finkbeiner, D. P., & Davis, M. 1998, *ApJ*, 500, 525, doi: [10.1086/305772](https://doi.org/10.1086/305772)
- Shapley, A. E., Reddy, N. A., Kriek, M., et al. 2015, *ApJ*, 801, 88, doi: [10.1088/0004-637X/801/2/88](https://doi.org/10.1088/0004-637X/801/2/88)
- Skillman, E. D., Salzer, J. J., Berg, D. A., et al. 2013, *AJ*, 146, 3, doi: [10.1088/0004-6256/146/1/3](https://doi.org/10.1088/0004-6256/146/1/3)
- Stanway, E. R., & Eldridge, J. J. 2018, *MNRAS*, 479, 75, doi: [10.1093/mnras/sty1353](https://doi.org/10.1093/mnras/sty1353)
- Steidel, C. C., Erb, D. K., Shapley, A. E., et al. 2010, *ApJ*, 717, 289, doi: [10.1088/0004-637X/717/1/289](https://doi.org/10.1088/0004-637X/717/1/289)
- Steidel, C. C., Strom, A. L., Pettini, M., et al. 2016, *ApJ*, 826, 159, doi: [10.3847/0004-637X/826/2/159](https://doi.org/10.3847/0004-637X/826/2/159)
- Steidel, C. C., Rudie, G. C., Strom, A. L., et al. 2014, *ApJ*, 795, 165, doi: [10.1088/0004-637X/795/2/165](https://doi.org/10.1088/0004-637X/795/2/165)
- Stevenson, C. C., McCall, M. L., & Welch, D. L. 1993, *ApJ*, 408, 460, doi: [10.1086/172603](https://doi.org/10.1086/172603)
- Storey, P. J., & Hummer, D. G. 1995, *MNRAS*, 272, 41, doi: [10.1093/mnras/272.1.41](https://doi.org/10.1093/mnras/272.1.41)
- Storey, P. J., Sochi, T., & Badnell, N. R. 2014, *MNRAS*, 441, 3028, doi: [10.1093/mnras/stu777](https://doi.org/10.1093/mnras/stu777)
- Strom, A. L., Steidel, C. C., Rudie, G. C., Trainor, R. F., & Pettini, M. 2018, *ApJ*, 868, 117, doi: [10.3847/1538-4357/aae1a5](https://doi.org/10.3847/1538-4357/aae1a5)
- Strom, A. L., Steidel, C. C., Rudie, G. C., et al. 2017, *ApJ*, 836, 164, doi: [10.3847/1538-4357/836/2/164](https://doi.org/10.3847/1538-4357/836/2/164)
- Strom, A. L., Rudie, G. C., Trainor, R. F., et al. 2023, *ApJL*, 958, L11, doi: [10.3847/2041-8213/ad07dc](https://doi.org/10.3847/2041-8213/ad07dc)
- Tayal, S. S. 2011, *ApJS*, 195, 12, doi: [10.1088/0067-0049/195/2/12](https://doi.org/10.1088/0067-0049/195/2/12)
- Tayal, S. S., & Zatsarinny, O. 2010, *ApJS*, 188, 32, doi: [10.1088/0067-0049/188/1/32](https://doi.org/10.1088/0067-0049/188/1/32)
- Thuan, T. X., Guseva, N. G., & Izotov, Y. I. 2022, *MNRAS*, 516, L81, doi: [10.1093/mnras/slac095](https://doi.org/10.1093/mnras/slac095)
- Thuan, T. X., Izotov, Y. I., & Lipovetsky, V. A. 1995, *ApJ*, 445, 108, doi: [10.1086/175676](https://doi.org/10.1086/175676)
- Topping, M. W., Shapley, A. E., Reddy, N. A., et al. 2020, *MNRAS*, 499, 1652, doi: [10.1093/mnras/staa2941](https://doi.org/10.1093/mnras/staa2941)
- Topping, M. W., Stark, D. P., Senchyna, P., et al. 2024, arXiv e-prints, arXiv:2401.08764, doi: [10.48550/arXiv.2401.08764](https://doi.org/10.48550/arXiv.2401.08764)
- Tosi, M. 1988, *A&A*, 197, 47
- Trainor, R. F., Steidel, C. C., Strom, A. L., & Rudie, G. C. 2015, *ApJ*, 809, 89, doi: [10.1088/0004-637X/809/1/89](https://doi.org/10.1088/0004-637X/809/1/89)
- Tremonti, C. A., Heckman, T. M., Kauffmann, G., et al. 2004, *ApJ*, 613, 898, doi: [10.1086/423264](https://doi.org/10.1086/423264)
- Trump, J. R., Arrabal Haro, P., Simons, R. C., et al. 2023, *ApJ*, 945, 35, doi: [10.3847/1538-4357/acba8a](https://doi.org/10.3847/1538-4357/acba8a)
- Vale Asari, N., Stasińska, G., Morisset, C., & Cid Fernandes, R. 2016, *MNRAS*, 460, 1739, doi: [10.1093/mnras/stw971](https://doi.org/10.1093/mnras/stw971)
- van Zee, L., & Haynes, M. P. 2006, *ApJ*, 636, 214, doi: [10.1086/498017](https://doi.org/10.1086/498017)
- Virtanen, P., Gommers, R., Oliphant, T. E., et al. 2020, *Nature Methods*, 17, 261, doi: [10.1038/s41592-019-0686-2](https://doi.org/10.1038/s41592-019-0686-2)

Welch, B., Olivier, G. M., Hutchison, T. A., et al. 2024, arXiv
e-prints, arXiv:2401.13046, doi: [10.48550/arXiv.2401.13046](https://doi.org/10.48550/arXiv.2401.13046)

Williams, H., Kelly, P. L., Chen, W., et al. 2023, *Science*, 380, 416,
doi: [10.1126/science.adf5307](https://doi.org/10.1126/science.adf5307)
Yates, R. M., Schady, P., Chen, T. W., Schweyer, T., & Wiseman,
P. 2020, *A&A*, 634, A107, doi: [10.1051/0004-6361/201936506](https://doi.org/10.1051/0004-6361/201936506)